



Porous PdZn bimettallene for oxygen reduction electrolysis

Hugang Zhang, Xinmiao Li, Yile Wang, Kai Deng, Hongjie Yu, You Xu, Hongjing Wang,
Ziqiang Wang*, Liang Wang*

State Key Laboratory Breeding Base of Green-Chemical Synthesis Technology, College of Chemical Engineering, Zhejiang University of Technology, Hangzhou 310014, PR China

ARTICLE INFO

Keywords:

PdZn bimettallene
Two-dimensional structure
Electronic effect
Oxygen reduction reaction
Zn-air battery

ABSTRACT

Two-dimensional (2D) Pd-based materials have been extensively researched as a cathode for oxygen reduction reaction (ORR) due to its distinctive physicochemical characteristics. In this paper, we report the controllable construction of porous wrinkled PdZn bimettallene (PdZn BMene) with the lattice distortions and grain boundaries via a one-step hydrothermal approach. Benefiting from the curved 2D metallene morphology, more sufficient and exposed active sites, and synergistic effect of alloy components, the resultant PdZn BMene exhibits outstanding ORR performance in 0.1 M KOH electrolyte, with the mass activity of $1.11 \text{ mA } \mu\text{g}_{\text{Pd}}^{-1}$, which is 1.6, 6.4, and 21.6 times higher than those of Pd metallene ($0.43 \text{ mA } \mu\text{g}_{\text{Pd}}^{-1}$), commercial Pt/C ($0.15 \text{ mA } \mu\text{g}_{\text{Pd}}^{-1}$), and Pd/C ($0.049 \text{ mA } \mu\text{g}_{\text{Pd}}^{-1}$), respectively. Moreover, PdZn BMene also possesses commendable durability, with only 7.2% activity loss after 30,000 potential cycles and a 5.3% attenuation of current density after 10-h durability test. Meanwhile, the assembled zinc-air battery with PdZn BMene as cathode catalyst possess an open-circuit voltage of 1.5 V and a maximum power density of 108.7 mW cm^{-2} along with benign durability. The present study highlights the advances of 2D Pd-based alloy bimettallene for realizing high-performance against the ORR application.

1. Introduction

To alleviate the environmental pollution and energy crisis, it is imperative to establish sustainable and promising electrochemical energy conversion devices, such as metal-air batteries [1–6]. The oxygen reduction reaction (ORR), as a key cathodic process in Zn-air batteries (ZABs), significantly limits the performance of batteries because of the sluggish kinetics [7,8]. To improve the performance and promote its practical application of ZABs, a considerable number of researches have been contributed to develop the ORR electrocatalysts with high activity and durability [9–12]. So far, Pt-based nanomaterials have been broadly considered as the benchmark of the ORR catalysts [13–15]. Nevertheless, Pt materials largely deters its widespread applications due to the susceptible poisoning to reaction intermediates and extreme scarcity [16,17]. Consequently, the advancement of non-Pt ORR electrocatalysts is extremely important, especially to achieve superior activity and durability at the same time, yet formidably challenging.

In general, as ORR electrocatalysts, implementing suitable chemisorption of O_2 while abolishing chemisorption of toxic species on the catalyst surface is an effective strategy to address this challenge. In view

of this, extensive research has been dedicated to developing the desirable ORR catalysts [18–20]. Among these, Pd-based catalysts have been intensively explored as a substitute for Pt in alkaline solutions because of the similar electronic and chemical properties [21–24]. Hitherto, a large number of diverse Pd-based nanostructures, such as the zero-dimensional (0D) nanoparticles [25,26], 1D nanotubes, nanowires and nanochains [27–29], 2D nanosheets and metallene [30,31], have been investigated toward the electrocatalytic ORR. Of all the distinct architectures of catalysts, metallene, as a newcomer of 2D materials, is established by bare metallic elements at a minority atomic scale, which can provide some irreplaceable superiorities including adequately exposed metal active sites, high conductivity and high atomic utilization, exhibiting the ever-growing attention for electrocatalytic applications and advanced energy devices [32–35]. Moreover, to further improve the performance of electrocatalyst, the generation of defects (e.g. grain boundaries, dislocations and vacancy defects) on the surface of nanocrystals according to regulate the morphology and composition of materials, is also an attractive strategy to influence catalytic performance [36,37]. For instance, Chen and his co-workers have pointed out that the lattice strain generated at the grain boundaries would change

* Corresponding authors.

E-mail addresses: zqwang@zjut.edu.cn (Z. Wang), wangliang@zjut.edu.cn (L. Wang).



the binding affinity towards oxygen species, which could lead to a change in the overall barrier for the entire path [38].

Motivated by the above deliberations, herein, the porous wrinkled PdZn alloy bimettallene (PdZn BMene) is successfully designed by a one-step solvothermal strategy. The as-developed PdZn BMene possess the highly curved and wrinkled structures with some lattice distortions and grain boundaries. The abundant active sites and unique mettallene structure have led to PdZn BMene that shows superior ORR performance in alkaline electrolyte with the mass activity (specific activity) of 1.11 mA $\mu\text{g}_{\text{Pd}}^{-1}$ (2.16 mA cm^{-2}) at 0.9 V versus reversible hydrogen electrode (RHE), which is higher than those of Pd metallene (0.43 mA $\mu\text{g}_{\text{Pd}}^{-1}$ and 1.01 mA cm^{-2}), commercial Pt/C (0.15 mA $\mu\text{g}_{\text{Pd}}^{-1}$ and 0.42 mA cm^{-2}), and Pd/C (0.049 mA $\mu\text{g}_{\text{Pd}}^{-1}$ and 0.18 mA cm^{-2}), respectively, and maintains well after 10-h durability test. Moreover, when the PdZn BMene is employed the air cathode, the assembled ZABs exhibit excellent battery performance.

2. Experimental section

2.1. Chemicals and materials

Sodium palladium (II) tetrachloride (Na_2PdCl_4), zinc acetylacetone hydrate ($\text{C}_{10}\text{H}_{14}\text{O}_4\text{Zn}\cdot\text{xH}_2\text{O}$, $\text{Zn}(\text{acac})_2$), diethylenetriamine (DETA), N, N-dimethylformamide (DMF), ethylene glycol (EG), potassium hydroxide (KOH), triethylenetetramine (TETA), ethanol ($\text{C}_2\text{H}_5\text{OH}$) and acetone were purchased from Aladdin. Commercial Pt/C (20 wt%) and Pd/C (10 wt%) were ordered from Alfa Aesar. Nafion 117 solution (5 wt%) was obtained from Sigma-Aldrich.

2.2. Synthesis of porous PdZn bimettallene

The porous PdZn bimettallene were prepared via a one-step solvothermal approach. Typically, we first prepared Na_2PdCl_4 solution in DMF (100 mM) and 100 mM of $\text{Zn}(\text{acac})_2$ DMF solution. Subsequently, 1.0 g of KOH, 5.8 mL of DMF solution, and 4.2 mL of EG solution were mixed in a 20-mL plastic vial to form a transparent solution under ultrasonication for 40 min. After this, 0.15 mL of $\text{Zn}(\text{acac})_2$ solution, 0.3 mL Na_2PdCl_4 solution, and 5.0 mL of DETA were successively added into the previous solution. The resultant solution was transferred to a sealed Teflon-lined stainless steel autoclave (25 mL), which was reacted for 6 h at 180 °C. Finally, the product was purified by centrifugation at 8000 rpm for 5 min and washed several times with acetone and ethanol. For comparison, Pd metallene was also prepared without the addition of Zn precursors under the similar conditions.

2.3. Material characterizations

Transmission electron microscopy (TEM) was carried out to observe the morphology and structure of the samples from a Hitachi HT 7700 at an operation voltage of 120 kV. In addition, high-resolution TEM (HRTEM), high-angle annular dark-field scanning transmission electron microscopy (HAADF-STEM), selected area electron diffraction (SAED) and elemental mapping images were conducted on a Talos S-FEG with an acceleration voltage of 200 kV. Atomic force microscopy (AFM) was featured on Bruker Dimension Icon in the peak force tapping mode. Scanning electron microscopy (SEM) was carried out on a ZEISS Gemini 500 at an accelerating voltage of 5 kV. X-ray powder diffraction (XRD, X'Pert PRO MPD) and X-ray photoelectron spectroscopy (XPS, Thermo ESCALAB 250XI) were employed to investigate the crystallographic data, surface electronic state and elemental composition of samples.

2.4. Electrochemical measurement

The electrocatalytic ORR performances of samples were measured by CHI 852D electrochemical analyzer equipped with a three-electrode system. For electrochemical measurements, the glassy carbon rotating

risk electrode (RDE) with a diameter of 3 mm, an Ag/AgCl (3 M KCl) electrode and Pt wire were utilized as the working electrode, the reference electrode and counter electrode, respectively. For the preparation of the working electrodes, the as-obtained products (2 mg) were completely dissolved in a mixture solution (1.0 mL) of water, isopropanol and Nafion (v/v/v = 0.7/0.2/0.1) by ultrasonication for 10 min to develop a well-distributed catalyst ink. Then, 2.5 μL of ink was cast on the surface of RDE and dried at room temperature.

The ORR tests were performed in O_2 -saturated 0.1 M KOH at a rotation rate of 1600 rpm with a sweep speed of 10 mV s^{-1} . Before the electrochemical tests, oxygen was fed into the 0.1 M KOH solution. Linear sweep voltammetry (LSV) were measured at a scan speed of 10 mV s^{-1} . The current density was normalized to the geometric area of the RDE (0.071 cm^2). Kinetic currents were calculated by using Koutecky-Levich equation:

$$j_k = \frac{j_l \times j}{j_l - j} \quad (1)$$

where j_k , j_l and j represent the kinetic current density, limited diffusion current density and measured current density, respectively.

The electrochemically active surface area (ECSA) of the catalysts was determined by integrating the PdO reduction peaks to find the coulombic charge over the cyclic voltammetry (CV) curves at room temperature in 0.1 M KOH solution with a scan rate of 50 mV s^{-1} , which was calculated according to the equation:

$$\text{ECSA} = \frac{Q(\mu\text{C} \bullet \text{cm}^{-2})}{Q_{\text{PdO}}(\mu\text{C} \bullet \text{cm}^{-2}) \times \text{Pd}_{\text{loading}}(\text{mg} \bullet \text{cm}^{-2}) \times 10} \quad (2)$$

where Q is the coulombic charge by integrating area of PdO reduction peak, $Q_{\text{PdO}} = 405 \mu\text{C} \cdot \text{cm}^{-2}$ is the charge value given for the reduction of a PdO monolayer, and $\text{Pd}_{\text{loading}}$ is the Pd mass loading on the electrodes.

The accelerated durability tests (ADT) were conducted in O_2 -saturated 0.1 M KOH solution by CV curves with a cyclic potential from 0.6 to 1.0 V under a sweeping rate of 100 mV s^{-1} for 30,000 cycles. The stability of the catalysts was tested by Chronoamperometric measurements at 0.6 V for 10 h. All mentioned potentials were calibrated with respect to the reversible hydrogen electrode (RHE) scale.

2.5. Zinc-air battery test

The electrochemical performance of the ZAB was carried out by a custom-made two-electrode Zn-air cell, using air as the cathode, polished Zn plate as the anode, and 6 M KOH solution as the electrolyte. The air cathode was composed of Ni foam, catalyst layer and gas diffusion layer. The well-dispersed catalyst ink was uniformly dropped onto Ni foam with a mass loading of 1 mg cm^{-2} (normalized to metal), and Ni foam was used as the corresponding current collector. As a comparison sample, Pt/C-NF, was prepared by dropping the commercial Pt/C catalyst ink on Ni foam to form a homogeneous catalyst layer with a loading amount of 1 mg cm^{-2} (normalized to Pt). LANHE CT2001A device was utilized for measuring the galvanostatic discharge of ZABs in an oxygen-saturated electrolyte, whereas CHI 660E workstation was used to test voltage-current polarization curves of ZABs with a scan speed of 5 mV s^{-1} .

3. Results and discussion

3.1. Synthesis and characterization of PdZn bimettallene

The porous wrinkled PdZn BMene is synthesized by a one-step solvothermal co-reduction approach in a mixture of DMF and EG at 180 °C for 6 h. As schematized in Fig. 1, Na_2PdCl_4 and $\text{Zn}(\text{acac})_2$ serve as metal precursors, and DETA serves as structural agent for the controlled growth of 2D bimettallene morphology. At the same time, KOH facilitates the decomposition of DMF into dimethylamine (DMA), which is also

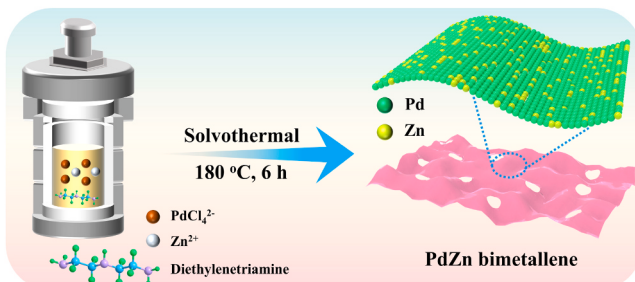


Fig. 1. Synthesis schematic view of PdZn bimettallene.

able to induce the formation of nanosheets structure during the continuous solvothermal reaction. Finally, the porous wrinkled PdZn BMene is constructed under synergistic effect of reactants and obtained by centrifugation and washing.

The morphology and structure of the porous wrinkled PdZn BMene was monitored by transmission electron microscopy (TEM) and high-angle annular dark field scanning transmission electron microscopy (HAADF-STEM). As displayed in Fig. 2a, the as-prepared catalyst holds 2D ultrathin graphene-like structures with lateral dimensions up to 500 nm. The magnified SEM and TEM images reveal that the nanosheets

appear bent, wrinkle, and folded morphology (Fig. S1 and Fig. 2b), signifying that it exhibits the high curvature and flexibility analogous to graphene, which may cause strain due to the curved geometry. TEM image further illustrates that the PdZn BMene possesses the 2D ultrathin nanosheets with the crimped surface, highly folded and wrinkled structures (Fig. 2c), which could lead to a shift of the d-band center away from the Fermi level and promote the suppression of poisoning species, thus strengthening the electrocatalytic property. The selected area electron diffraction (SAED) pattern displays four clear concentric rings corresponding to the (111), (200), (220), and (311) diffraction facets of the PdZn BMene (inset in Fig. 2c), revealing its polycrystalline nature. For contrast, the Pd metallene was also simultaneously prepared by using the same method without the addition of Zn precursor. It can be clearly observed from Fig. S2 and S3 that Pd metallene possess a similar morphology and structure as PdZn BMene. Furthermore, atomic force microscopy (AFM) was utilized to measure the thickness of PdZn BMene. As shown in Fig. 2d, the height profile is determined to be ~1.56 nm, which could greatly ameliorate the catalytic activity because the intrinsic strain of 2D metals with thin atomic thickness can effectively regulate the surface electron energy and structure of the reaction intermediates. The perforated structure of PdZn BMene can be clearly observed in high-magnification HAADF-STEM image (Fig. 2e), which could not only favor mass and electron transfer, but also provide

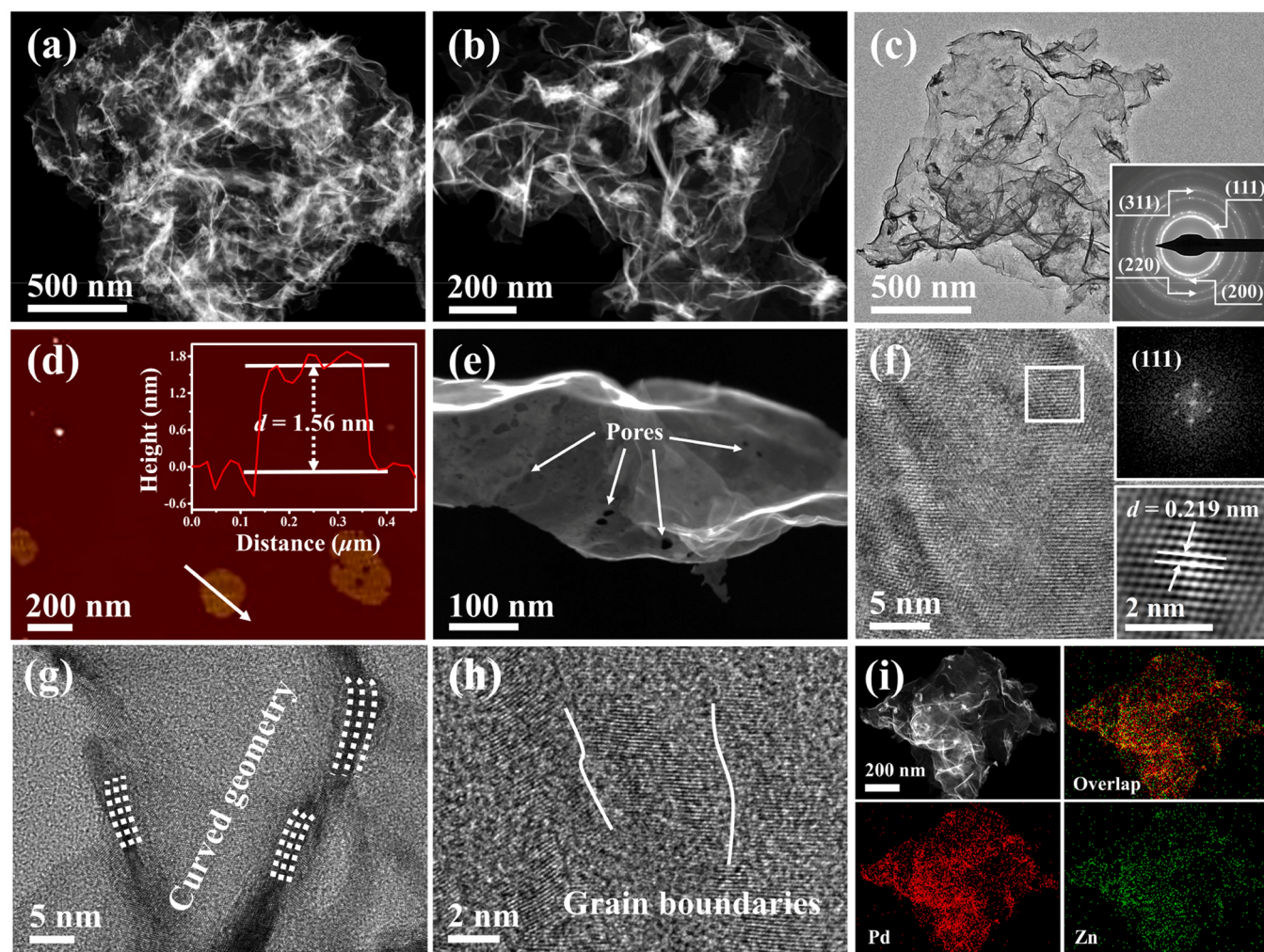


Fig. 2. (a and b) Low and high-magnification HAADF-STEM images, (c) TEM images and the inset in (c) is the SAED pattern, (d) AFM image and the corresponding height profile, (e) high-magnification HAADF-STEM image, (f) HRTEM image and the insets in (f) are the corresponding FFT pattern and the lattice distance, (g) HRTEM image from folded edge region, (h) HRTEM image from lateral region, and (i) HAADF-STEM image and the corresponding EDX mapping images of the PdZn bimettallene.

unsaturated atoms and high specific surface area, thus facilitating electrocatalytic properties [34]. From the high-resolution TEM (HRTEM) image of PdZn BMene (Fig. 2 f), the (111) crystal facet is confirmed by the fast Fourier transform (FFT) pattern of the square area (inset in Fig. 2 f) and the corresponding *d*-spacing of lattice fringes is measured to be 0.219 nm, corresponding to the (111) planes of the Pd-based face-centered cubic (fcc) structure. It is noteworthy that the lattice spacing of PdZn BMene is slightly smaller than that of Pd metallene (0.221 nm, Fig. S2d), which is ascribed to the incorporation of Zn element. In addition, the distortion of lattice fringes can be clearly observed according to the folded edge region in the HRTEM image (Fig. 2 g), which is further proved the curved geometry of PdZn BMene. Meanwhile, several grain boundaries are also observed from the lateral region in PdZn BMene (Fig. 2 h). Noteworthy, these lattice distortions and grain boundaries could deliver a large number of defect sites (Fig. S4), which have been evidenced to facilitate the electrocatalytic activity [39,40]. HAADF-STEM image and the corresponding element mapping images (Fig. 2i) prove that Pd and Zn atoms are homogeneously dispersed throughout the PdZn BMene with a composition ratio of 81.9/18.1 determined by energy dispersive X-ray spectroscopy (EDX) measurement (Fig. S5).

The crystalline structures of samples were characterized by XRD pattern (Fig. 3a). The as-synthesized PdZn BMene presents four characteristic diffraction patterns locating at 40.3°, 46.8°, 68.3°, and 82.3° of 2θ values corresponding to the (111), (200), (220), and (311) crystal-planes of fcc Pd structure (JCPDS card no. 46–1043), which are matched very well with the results of the SAED pattern. Compared to the Pd metallene, the diffraction peaks of PdZn BMene are deviated to a higher 2θ values due to the introduction of smaller Zn atom into the Pd lattice, indicating a contraction of the lattice parameter, which could induce compressive strain effect, agreeing with the analysis of HRTEM. The electronic structures and surface constituents of the PdZn BMene were further investigated by XPS technology. As shown in Fig. 3b, the broad survey spectrum verifies the existence of Pd, Zn and O elements in the PdZn BMene. In the high-resolution Pd 3d spectrum (Fig. 3c), two fitted

peaks at 340.1 and 334.9 eV can be assigned to the Pd 3d_{3/2} and Pd 3d_{5/2} of metallic Pd in the PdZn BMene, respectively, while the other weak peaks situated at 341.0 eV (Pd 3d_{3/2}) and 336.3 eV (Pd 3d_{5/2}) are indexed to the Pd(II) [41,42]. As for the high-resolution Zn 2p XPS signals (Fig. 3d), one pair of the visible peaks of PdZn BMene at 1044.2 and 1020.8 eV belong to the spin-orbit doublet Zn 2p_{1/2} and Zn 2p_{3/2} of Zn(II) [43]. Specifically, it can be observed that the relevant binding energy of Pd 3d for PdZn BMene displays a positive 0.2 eV shift compared with the Pd metallene due to the incorporation of Zn, which could cause a downshift of the d-band center of Pd and adjust adsorption energy of oxygenated species, thereby enhancing the electrocatalytic ORR activity [44–46].

3.2. The effect of synthetic factors on PdZn bimettallene

To shed light on the roles of synthetic factors on the construction of the PdZn BMene, a set of the reaction parameters experiments were carried out. The function of DETA in the reaction mixture was investigated by altering the amount and substitute. In the absence of DETA, irregularly agglomerated nanoparticles could be achieved (Fig. S6a). The nanosheets structure gradually started to form when a small amount of DETA (1 mL) was introduced into the system (Fig. S6b). The well-defined mettallene morphology was obtained by reaching 5 mL of the DETA content. When the amount of DETA was increased to 10 mL, no obvious variation was observed in the laminar architecture (Fig. S6c). These analyses indicate that DETA plays a significant role in the guiding growth of 2D nanosheets this is because DETA can chelate with Pd²⁺ and Zn²⁺ to form ligand compounds, which could retard the reduction rate of the metal precursor and avert supersaturation and stochastic nucleation of nanoparticles, thereby facilitating selective growth into nanosheets [47]. Additionally, when using other polyamine ligand (triethylenetetramine, TETA) to replace DETA (Fig. S7), the PdZn nanosheet with the laminar architecture can also be produced. The influence of KOH amount on the growth of nanosheets structure was investigated. In the absence of KOH, only large agglomerated

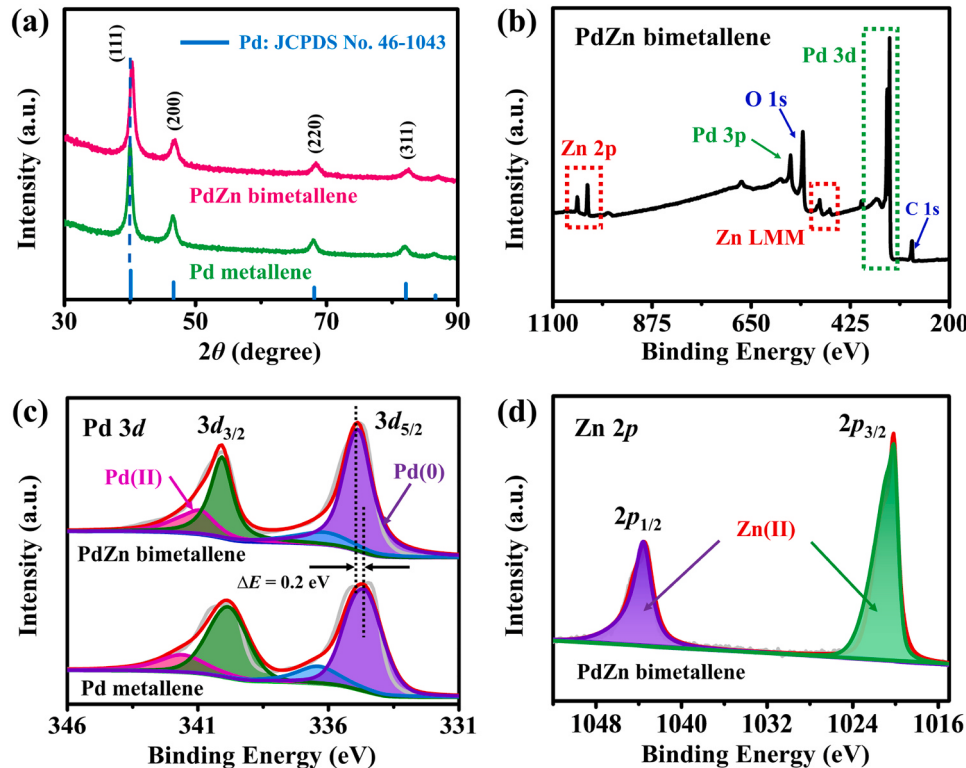


Fig. 3. (a) XRD pattern, (b) XPS survey spectrum, and high-resolution XPS spectra of (c) Pd 3d and (d) Zn 2p for PdZn bimettallene.

nanostructures were formed (Fig. S8a). When a small amount of KOH (0.1 g) was added to the reaction system, nanoparticle aggregates and nanosheets were simultaneously procured (Fig. S8b). With the increase of KOH, the nanosheet structure becomes more pronounced and the number of nanoparticles decreased (Fig. S8c). It is known that KOH could facilitate the decomposition of DMF at the appropriate temperature and produce DMA, which plays an important role in controlling the growth of facet and forming a porous structure [48]. The samples with different proportions of Pd and Zn precursors are prepared to explore their effect on morphology of PdZn BMene. As observed in Fig. S9a, only Pd metallene is generated without the addition of Zn precursor. The well-developed PdZn BMene is synthesized under the condition that the precursor ratio of Pd and Zn is 3:1. With the increasing content of Zn precursors, the nanoparticles start to appear and then become progressively more apparent (Fig. S9b and c), revealing that the Zn precursor is superfluous. A considerable number of irregularly agglomerated nanoparticles are obtained when only Zn(acac)₂ is added to the reaction (Fig. S9d). Consequently, the Pd precursor is of crucial importance to the formation of 2D metallene structure in this system and the proposed preparation approach has a high guiding role in the synthesis of other Pd-based bimettallene.

Furthermore, the time-related experiments were conducted to trap the formation mechanism of the PdZn BMene. As illustrated in Fig. S10a, when the reaction just commences for 5 min, there is the formation of most aggregated nanoparticles and a small number of nanosheets in the edge portion. When the reaction proceeds to 30 min, abundant nanosheets and small aggregated nanoparticles can be observed (Fig. S10b). As the reaction time is sustained for 2 h, the nanosheet structure is developed, accompanied with few agglomerated nanoparticles (Fig. S10c). When the reaction time is up to 5 h, the resultant samples with the well-defined and wrinkled 2D metallene structure have been thoroughly produced without any nanoparticles (Fig. S10d). To assure that the precursors added to the reaction are exhaustively reduced, 6 h is eventually employed as a typical reaction time.

3.3. ORR electroactivity of PdZn bimettallene

Given the unique mettallene structure and compositional characteristics, we employ the ORR in 0.1 M KOH as a model reaction to assess the electrocatalytic activity of the PdZn BMene and benchmark their performance against the Pd metallene, commercial Pt/C, and Pd/C catalyst. Cyclic voltammetry (CV) curves of samples were first tested in N₂-saturated 0.1 M KOH solution at the potential between 0 and 1.2 V. As shown in Fig. S11a, the samples containing Pd exhibit analogous electrochemical behavior in CV curves, where the cathodic peak related to Pd reduction (reduction of Pd-OH_{ad}) can be obviously identified in the potential range of 0.65–0.85 V. Apparently, compared to Pd/C, the Pd-OH_{ad} reduction peak of PdZn BMene possesses a positive deviation of 71 mV, suggesting a weaker oxygen affinity and possibly favoring ORR [45,46]. In comparison, Pt/C manifests a distinct electrochemical behavior with more symmetrical redox peaks for the underpotential adsorption and desorption of hydrogen and Pt-OH (Fig. S11b). Furthermore, the ECSAs of Pd-containing catalysts and Pt/C are calculated from the area of the reduction peak of PdO and the hydrogen adsorption peak of Pt/C, respectively, and the value of PdZn BMene (51.4 m² g⁻¹_{Pd}) is higher than that of Pd metallene (42.5 m² g⁻¹_{Pd}), Pd/C (27.3 m² g⁻¹_{Pd}), and Pt/C (35.6 m² g⁻¹_{Pt}), which is mainly ascribed to porous wrinkled structures (Fig. S12).

The electrocatalytic ORR activity of all catalysts was explored by linear sweep voltammogram (LSV) performed in O₂-saturated 0.1 M KOH solution at a sweep rate of 10 mV s⁻¹ and a rotation rate of 1600 rpm. Fig. 4a presents LSV curves of ORR for various catalysts at room temperature. It can be observed that PdZn BMene has a more positive reduction potential and a larger limiting current density compared to Pd metallene, Pt/C, and Pd/C, revealing that the introduction of Zn could ameliorate the performance towards the ORR. As seen from the ORR polarization curves, the onset potential (E_{onset}) and half-wave potential ($E_{1/2}$) potentials of PdZn BMene are 1.13 and 1.05 V, respectively, which are considerably higher than those of Pd metallene (1.09 and 1.01 V), Pd/C (1.07 and 0.95 V) and Pt/C (1.01 and 0.92 V) (Fig. 4b), indicating that PdZn BMene possess the superior ORR

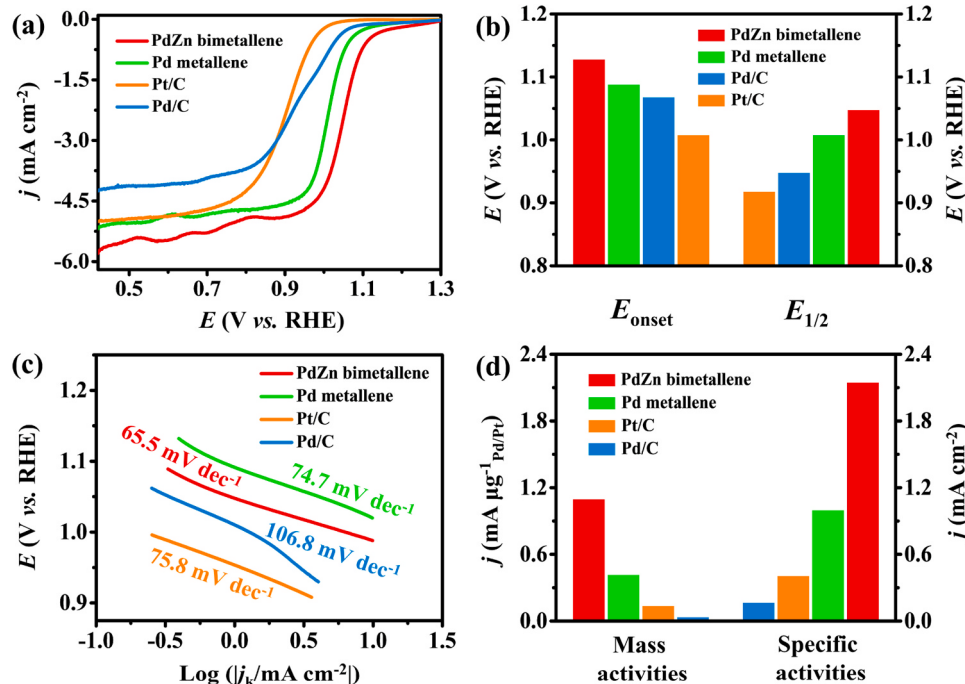


Fig. 4. (a) ORR polarization curves in an O₂-saturated 0.1 M KOH solution with a rotation rate of 1600 rpm at a scan speed of 10 mV s⁻¹. (b) The E_{onset} and $E_{1/2}$ for different samples. (c) Tafel slopes derived from polarization curves for the catalysts. (d) The comparison of mass activity and specific activity at 0.9 V for different samples.

performance. Additionally, PdZn BMene has a larger limiting diffusion current relative to Pd metallene, Pt/C, and Pd/C, which is because the higher active surface area of PdZn BMene increases the number of sites available for the diffusion of reactants and products, leading to higher rate of diffusion. Tafel slope by fitting LSV curves as an important evaluation for the ORR activity was applied to investigate the reaction kinetics. As shown in Fig. 4c, the Tafel slope of PdZn BMene is 65.5 mV dec⁻¹, which is much lower than that of Pd metallene (74.7 mV dec⁻¹), Pt/C (75.8 mV dec⁻¹), and Pd/C (106.8 mV dec⁻¹), demonstrating that PdZn BMene has a faster dynamics property during the ORR process. Additionally, electrochemical impedance spectroscopy (EIS) techniques were employed to understand the ORR electron transfer kinetics happening at the electrode/electrolyte interface. The Nyquist plots of the studied electrocatalysts are derived from the EIS data with the fitted equivalent circuits in O₂-saturated 0.1 M KOH solution (Fig. S13). It can be seen that PdZn BMene has the smallest semicircular arc, attesting its smallest charger-transfer resistance (R_{ct}) for ORR. This is because Zn is an antioxidative element and has the higher electron density, which contributes to the higher electronic conductivity of PdZn BMene catalyst than Pd metallene, Pt/C, and Pd/C. The R_{ct} of PdZn BMene is determined to 166.6 Ω, which is remarkably smaller than those of Pd metallene (265.2 Ω), Pt/C (328.5 Ω), and Pd/C (399.1 Ω) (More detailed data see Table S1), indicating the enhanced conductivity of PdZn BMene. To

further reveal the intrinsic activity of electrocatalysts, the kinetic currents of samples at 0.9 V_{RHE} were estimated from the polarization curves using the Koutecky-Levich (K-L) equation, and then the mass activity (MA) and specific activity (SA) were yielded by normalizing kinetic current to the metal mass and ECSA, respectively. Conspicuously, PdZn BMene displays the highest MA and SA values of 1.11 mA μg_{Pd}⁻¹ and 2.16 mA cm⁻², which are preferable to those of Pd metallene (0.43 mA μg_{Pd}⁻¹ and 1.01 mA cm⁻²), Pt/C (0.15 mA μg_{Pd}⁻¹ and 0.42 mA cm⁻²), and Pd/C (0.049 mA μg_{Pd}⁻¹ and 0.18 mA cm⁻²) (Fig. 4d). It is imperative to note that the ORR activity of PdZn BMene is better than that of most reported Pd-based electrocatalysts (Table S2). In the interest of understanding the ORR mechanism, rotation-rate-associated polarization curves of PdZn BMene catalyst were performed at different RDE rotation rates (625–2025 rpm). As depicted in Fig. S14a, the current density of PdZn BMene follows a regular variation at different rotation rates. The corresponding K-L plots at four continuous potentials (0.5–0.65 V) almost overlap, manifesting the first-order reaction kinetics for the ORR (Fig. S14b). And the electron transfer number (n) of PdZn BMene at each potential is calculated to be approximately 4, confirming the four-electron transfer pathway on PdZn BMene with the full conversion of oxygen to OH⁻.

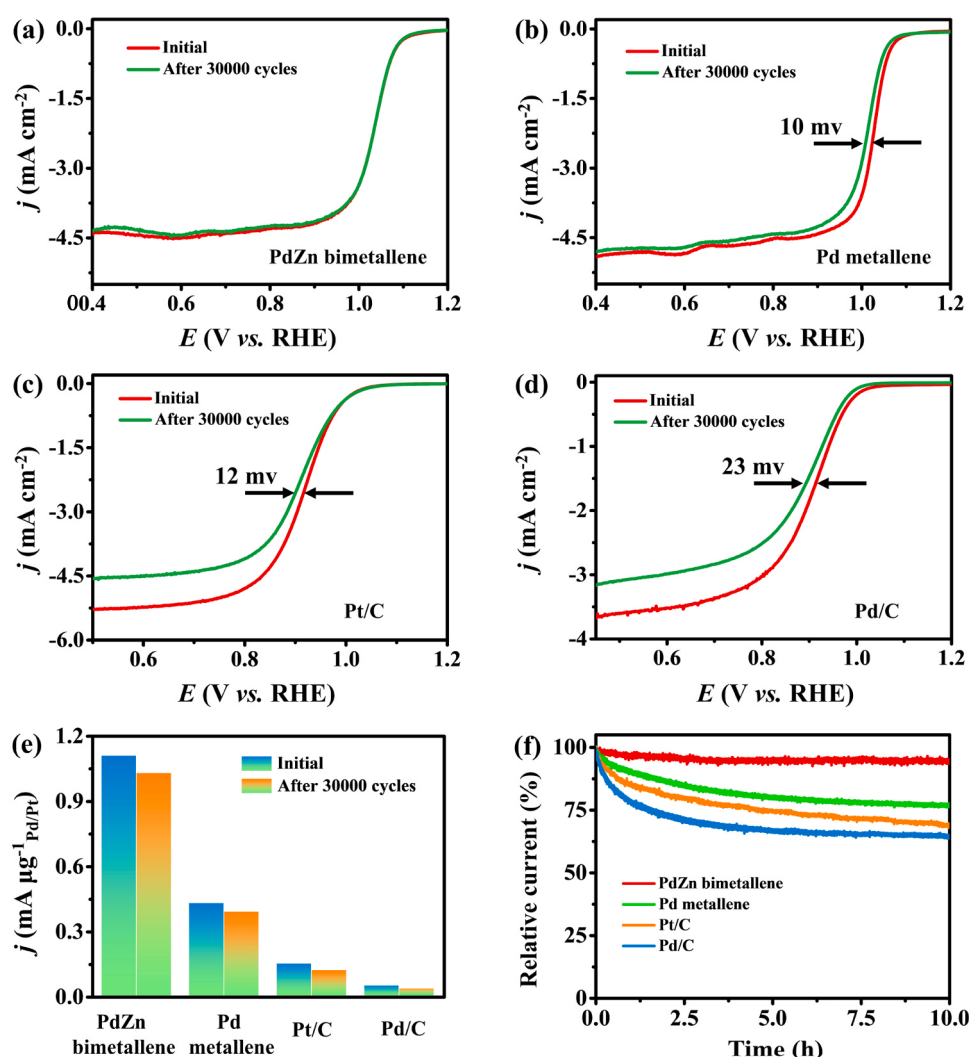


Fig. 5. ORR polarization curves of (a) PdZn metallene, (b) Pd metallene, (c) Pt/C, and (d) Pd/C at a rotation rate of 1600 rpm and a scan rate of 10 mV s⁻¹ before and after 30,000 potential cycles. (e) Changes in mass activities of the studied electrocatalysts before and after ADT test. (f) Chronoamperometric measurements of the catalysts at 0.6 V for 10 h in an O₂-saturated 0.1 M KOH solution at a rotation rate of 1600 rpm.

3.4. ORR stability of PdZn bimettallene

The stability and durability, as key indicators for measuring ORR electrocatalysts, play an essential role in practical applications. The electrochemical accelerated durability test (ADT) was carried out to judge the stability of samples according to circulate the potential between 0.6 and 1.0 V in O₂-saturated 0.1 M KOH electrolyte at room temperature. As shown in Fig. 5a-d, after 30,000 cycles of consecutive potential cycles, the polarization curve of PdZn BMene possess a negligible activity attenuation in $E_{1/2}$ and the limiting current density, while Pd metallene, Pt/C, and Pd/C exhibit a noticeable $E_{1/2}$ decay by 10, 12, and 23 mV, respectively. To be more quantified, the MA evolution of samples was determined after stability testing. As charted in Fig. 5e, the MA of PdZn BMene decreases to 1.03 mA $\mu\text{g}_{\text{Pd}}^{-1}$, only 7.2% smaller than the initial activity, which is in stark contrast with those of Pd metallene (9.3% loss), Pt/C (20% loss), and Pd/C (28.6% loss) after 30,000 potential cycles. Moreover, the long-term durability of the studied electrocatalysts was corroborated by chronoamperometric measurement at 0.6 V for 10 h in an O₂-saturated 0.1 M KOH solution with a rotation rate of 1600 rpm. As illustrated in Fig. 5f, the ORR current density of PdZn BMene only attenuates 5.3% after 10-h durability test, which is better than Pd metallene (23.1%), Pt/C (31.3%), and Pt/C (35.7%). After the stability test, it can be proved by SEM, HAADF-STEM and TEM images that PdZn BMene has no obvious change in morphology and

structure (Fig. S15). These foregoing analyses confirm the outstanding stability and durability of PdZn BMene.

The highly enhanced electrocatalytic activity and stability of PdZn BMene could be ascribed to as below. First, the ultrathin 2D metallene geometric architecture has larger specific surface and higher ECSA, which could provide more sufficient and exposed active sites for ORR. Moreover, the lattice distortions and grain boundaries in the PdZn BMene could potentially deliver a large number of defect sites, which is able to facilitate the electrocatalytic ORR activity [33,49]. Second, the highly folded and wrinkled structures could lead to a downshift of the d-band center and promote the suppression of poisoning species [34], thus strengthening the electrocatalytic property. And the perforated structure with numerous pores could promote electron transfer and improve mass transport. Third, the incorporation of Zn causes a downshift of the d-band center of Pd and modulate the electron structure change between Pd and Zn, which could adjust adsorption energy of oxygenated species, thereby enhancing the electrocatalytic ORR activity. Finally, the wrinkled structure is conducive to the high stabilities of catalyst due to prevent the aggregation or stacking of the layers during the ORR process [47]. And the strong electronic effect between Pd and Zn can also effectively impede the dissolution of Pd, thereby resulting in the excellent stability.

Due to the outstanding ORR performance, the as-fabricated PdZn BMene was served as electrode material for primary Zn-air battery.

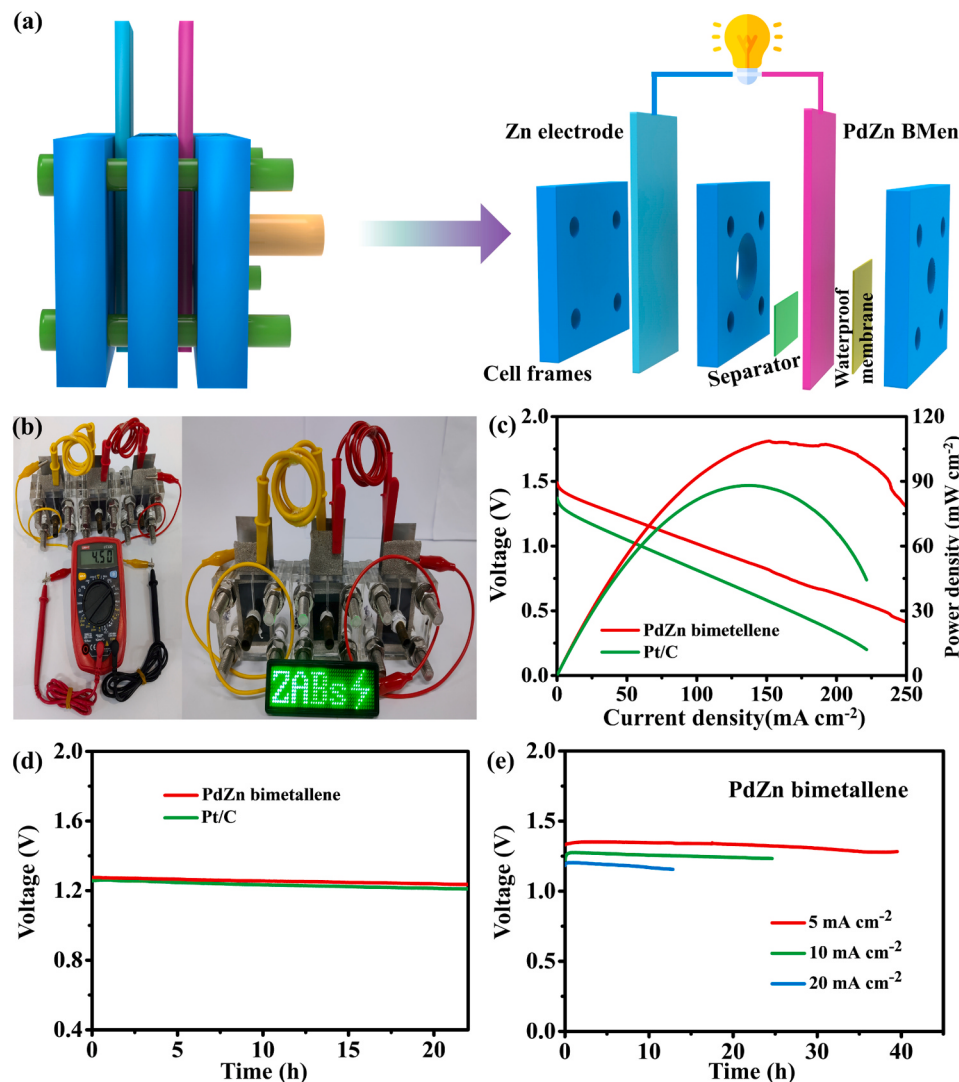


Fig. 6. (a) Schematic configuration of the structure of the primary ZAB. (b) Photographs of an open-circuit potential of 4.5 V and a small green LED screen (3.7 V) powered by three ZABs in series. (c) LSV curves and power densities of the Zn-air battery by using PdZn BMene and Pt/C catalysts as the air electrode, respectively. (d) Long-term discharge curves of the samples. (e) Galvanostatic discharge curves of the ZAB assembled by the PdZn BMene at various current densities (5, 10, and 20 mA cm⁻²).

Fig. 6a exhibits the schematic configuration of a home-built ZAB, which is assembled by utilizing the PdZn BMene catalyst on the gas diffusion layer as the air cathode, polished Zn plate as the anode, and 6 M KOH solution as the electrolyte, respectively. As shown in **Fig. 6b**, three series-wound ZABs equipped with the PdZn BMene as cathode could perform high open-circuit voltage (OCV) of 4.5 V, indicating the average OCV of 1.5 V for single battery, which can effectively drive a diminutive green light-emitting diode (LED) panel with a rated voltage of 3.7 V. For comparison, the commercial Pt/C was also evaluated as cathode catalyst for ZAB under the identical conditions. The polarization discharged curves and power density curves utilizing PdZn BMene and Pt/C catalysts were first investigated (**Fig. 6c**). The ZAB assembled by the PdZn BMene possesses the OCV of 1.5 V and maximum power density of 108.7 mW cm^{-2} , which are higher than those of the Pt/C-based ZAB (OCV of 1.37 V and power density of 88.1 mW cm^{-2}). Moreover, the galvanostatic discharge curves were tested at a current density of 10 mA cm^{-2} . It can be seen from **Fig. 6d** that the PdZn BMene exhibits an open circuit potential as high as 1.276 V at 10 mA cm^{-2} , which is slightly higher than that of the commercial Pt/C (1.256 V). And the discharge voltage of the ZAB assembled by the PdZn BMene catalyst is retained after 22 h operation. In addition, the galvanostatic discharge curves of the PdZn BMene at different current densities were also investigated (**Fig. 6e**). The discharge voltage is stable after 40 and 12 h tests at 5 and 20 mA cm^{-2} , respectively. These above experimental results clearly demonstrate that the as-prepared PdZn BMene catalyst has excellent catalytic performance and stability in practical applications for ZABs.

4. Conclusion

In summary, we have been successfully developed the highly porous, wrinkled and ultrathin PdZn alloy bimallene by a one-step solvothermal co-reduction approach. A series of electrocatalytic studies indicate that the MA and SA of as-fabricated PdZn BMene catalyst towards the ORR in alkaline electrolyte remarkably outperform those of Pd metallene, commercial Pt/C, and Pd/C, while PdZn BMene exhibits the excellent stability after 30,000 potential cycles and 10-h long-term test. The enhanced ORR electrochemical performance is mainly ascribed to the ultrathin 2D metallene geometric architecture, more sufficient and exposed active sites, synergistic effect of bimetallic components, and modulated electronic structure. Moreover, the assembled zinc-air battery with PdZn BMene as cathode catalyst possess an open-circuit voltage of 1.5 V and a maximum power density of 108.7 mW cm^{-2} along with benign durability. The present work provides an effective strategy for guiding the design and preparation of ultrathin 2D Pd-based bimallene electrocatalysts with desired morphologies and components, which would favor the improvement of activity and durability towards energy conversion applications and beyond.

CRediT authorship contribution statement

Hugang Zhang: Experimental Measurements, Data Analysis, Manuscript Preparation. **Xinmiao Li:** Experimental Measurements, Data Analysis. **Yile Wang:** Data Analysis. **Kai Deng:** Visualization. **Hongjie Yu:** Formal analysis. **You Xu:** Writing – review & editing. **Hongjing Wang:** Supervision, Formal analysis, Funding acquisition. **Ziqiang Wang:** Writing – review & editing, Supervision, Project administration. **Liang Wang:** Conceptualization, Writing – review & editing, Supervision, Project administration.

Declaration of Competing Interest

The authors declare that they have no known competing financial interests or personal relationships that could have appeared to influence the work reported in this paper.

Data Availability

No data was used for the research described in the article.

Acknowledgements

This work was financially supported by the National Natural Science Foundation of China (Nos. 21972126, 21978264, 21905250 and 22278369), Natural Science Foundation of Zhejiang Province (No. LQ22B030012 and LQ23B030010), and China Postdoctoral Science Foundation (2021M702889).

Appendix A. Supporting information

Supplementary data associated with this article can be found in the online version at doi:[10.1016/j.apcatb.2023.123006](https://doi.org/10.1016/j.apcatb.2023.123006).

References

- [1] Z.W. Seh, J. Kibsgaard, C.F. Dickens, I. Chorkendorff, J.K. Nørskov, T.F. Jaramillo, Combining theory and experiment in electrocatalysis: Insights into materials design, *Science* 355 (2017) eaad4998, doi:[10.1126/science.aad4998](https://doi.org/10.1126/science.aad4998).
- [2] D. Shindell, C.J. Smith, Climate and air-quality benefits of a realistic phase-out of fossil fuels, *Nature* 573 (2019) 408–411, <https://doi.org/10.1038/s41586-019-1554-z>.
- [3] P. Wang, Y. Luo, G. Zhang, M. Wu, Z. Chen, S. Sun, Z. Shi, MnO_x-decorated Nickel-iron phosphides nanosheets: Interface modifications for robust overall water splitting at ultra-high current densities, *Small* 18 (2022) 2105803, <https://doi.org/10.1002/smll.202105803>.
- [4] X. Liu, G. Zhang, L. Wang, H. Fu, Structural design strategy and active site regulation of high-efficient bifunctional oxygen reaction electrocatalysts for Zn-air battery, *Small* 17 (2021) 2006766, doi:[10.1002/smll.202006766](https://doi.org/10.1002/smll.202006766).
- [5] D. Liu, A. Barbar, T. Najam, M.S. Javed, J. Shen, P. Tsakarous, X. Cai, Single noble metal atoms doped 2D materials for catalysis, *Appl. Catal. B Environ.* 297 (2021), 120389, <https://doi.org/10.1016/j.apcatb.2021.120389>.
- [6] W. Li, Z. Guo, J. Yang, Y. Li, X. Sun, H. He, S. Li, J. Zhang, Advanced strategies for stabilizing single-atom catalysts for energy storage and conversion, *Electrochim. Energy Rev.* 5 (2022) 9, <https://doi.org/10.1007/s41918-022-00169-z>.
- [7] H.-F. Wang, C. Tang, Q. Zhang, A review of precious-metal-free bifunctional oxygen electrocatalysts: rational design and applications in Zn-air batteries, *Adv. Funct. Mater.* 28 (2018) 1803329, <https://doi.org/10.1002/adfm.201803329>.
- [8] J. Yan, F. Ye, Q. Dai, X. Ma, Z. Fang, L. Dai, C. Hu, Recent progress in carbon-based electrochemical catalysts: from structure design to potential applications, *Nano Res. Energy* 2 (2023) 9120047, <https://doi.org/10.26599/NRE.2023.9120047>.
- [9] X. Tian, X.F. Lu, B.Y. Xia, X.W. Lou, Advanced electrocatalysts for the oxygen reduction reaction in energy conversion technologies, *Joule* 4 (2020) 45–68, <https://doi.org/10.1016/j.joule.2019.12.014>.
- [10] X. Wang, Z. Li, Y. Qu, T. Yuan, W. Wang, Y. Wu, Y. Li, Review of metal catalysts for oxygen reduction reaction: from nanoscale engineering to atomic design, *Chem* 5 (2019) 1486–1511, <https://doi.org/10.1016/j.chempr.2019.03.002>.
- [11] J. Xu, S. Lai, D. Qi, M. Hu, X. Peng, Y. Liu, W. Liu, G. Hu, H. Xu, F. Li, C. Li, J. He, L. Zhuo, J. Sun, Y. Qiu, S. Zhang, J. Luo, X. Liu, Atomic Fe-Zn dual-metal sites for high-efficiency pH-universal oxygen reduction catalysis, *Nano Res.* 14 (2020) 1374–1381, <https://doi.org/10.1007/s12274-020-3186-x>.
- [12] X. Hu, Y. Min, L.-L. Ma, J.-Y. Lu, H.-C. Li, W.-J. Liu, J.-J. Chen, H.-Q. Yu, Iron-nitrogen doped carbon with exclusive presence of Fe_xN active sites as an efficient ORR electrocatalyst for Zn-air battery, *Appl. Catal. B Environ.* 268 (2020), 118405, <https://doi.org/10.1016/j.apcatb.2019.118405>.
- [13] H. Liu, J. Zhao, X. Li, Controlled synthesis of carbon-supported Pt-based electrocatalysts for proton exchange membrane fuel cells, *Electrochim. Energy Rev.* 5 (2022) 13, <https://doi.org/10.1007/s41918-022-00173-3>.
- [14] X.-L. Liu, Y.-C. Jiang, J.-T. Huang, W. Zhong, B. He, P.-J. Jin, Y. Chen, Bifunctional PdPt bimallenes for formate oxidation-boosted water electrolysis, *Carbon Energy* (2023), e367, <https://doi.org/10.1002/cey2.367>.
- [15] Z. Ma, Z.P. Cano, A. Yu, Z. Chen, G. Jiang, X. Fu, L. Yang, T. Wu, Z. Bai, J. Lu, Enhancing oxygen reduction activity of Pt-based electrocatalysts: From theoretical mechanisms to practical methods, *Angew. Chem. Int. Ed.* 59 (2020) 18334–18348, <https://doi.org/10.1002/anie.202003654>.
- [16] Y. Qin, W. Zhang, K. Guo, X. Liu, J. Liu, X. Liang, X. Wang, D. Gao, L. Gan, Y. Zhu, Z. Zhang, W. Hu, Fine-tuning intrinsic strain in penta-twinned Pt-Cu-Mn nanoframes boosts oxygen reduction catalysis, *Adv. Funct. Mater.* 30 (2020) 1910107, <https://doi.org/10.1002/adfm.201910107>.
- [17] X. Wang, J. Li, X. Yang, F. Zhao, Y. Li, D. Zhang, L.-Y. Gan, K.X. Yao, Q. Yuan, Low-coordinated surface sites make truncated Pd tetrahedrons as robust ORR electrocatalysts outperforming Pt for DMFC devices, *Nano Res.* 15 (2022) 7951–7958, <https://doi.org/10.1007/s12274-022-4492-2>.
- [18] H. Xie, S. Chen, J. Liang, T. Wang, Z. Hou, H.-L. Wang, G. Chai, Q. Li, Weakening intermediate bindings on CuPd/Pd core/shell nanoparticles to achieve Pt-Like bifunctional activity for hydrogen evolution and oxygen reduction reactions, *Adv. Funct. Mater.* 31 (2021) 2100883, <https://doi.org/10.1002/adfm.202100883>.

[19] L. Bu, S. Guo, X. Zhang, X. Shen, D. Su, G. Lu, X. Zhu, J. Yao, J. Guo, X. Huang, Surface engineering of hierarchical platinum–cobalt nanowires for efficient electrocatalysis, *Nat. Commun.* 7 (2016) 11850, <https://doi.org/10.1038/ncomms11850>.

[20] X. Tong, X. Zhan, D. Rawach, Z. Chen, G. Zhang, S. Sun, Low-dimensional catalysts for oxygen reduction reaction, *Prog. Nat. Sci.: Mater. Int.* 30 (2020) 787–795, <https://doi.org/10.1016/j.pnsc.2020.09.011>.

[21] Q. Li, X. Wang, Z. Xie, X. Peng, L. Guo, X. Yu, X. Yang, Z. Lu, X. Zhang, L. Li, Polar bonds induced strong Pd-support electronic interaction drives remarkably enhanced oxygen reduction activity and stability, *Appl. Catal. B Environ.* 305 (2022), 121020, <https://doi.org/10.1016/j.apcatb.2021.121020>.

[22] T. Wang, A. Chutia, D.J.L. Brett, P.R. Shearing, G. He, G. Chai, I.P. Parkin, Palladium alloys used as electrocatalysts for the oxygen reduction reaction, *Energy Environ. Sci.* 14 (2021) 2639–2669, <https://doi.org/10.1039/d0ee03915b>.

[23] M. Ma, Y. Zhang, Y. Ji, Q. Shao, K. Yin, W. Zhu, J. Yang, F. Liao, Z. Fan, Y. Liu, Y. Li, M. Shao, Z. Kang, Diluted silicon promoting Pd/Pt catalysts for oxygen reduction reaction with strong anti-poisoning effect, *Appl. Catal. B Environ.* 315 (2022), 121549, <https://doi.org/10.1016/j.apcatb.2022.121549>.

[24] Z. Wang, P. Tian, H. Zhang, K. Deng, H. Yu, X. Wang, Y. Xu, H. Wang, L. Wang, Phosphorus-triggered activation of PdPb nanoflowers for enhanced oxygen reduction electrocatalysis, *J. Mater. Chem. A* 10 (2022) 15528–15534, <https://doi.org/10.1039/d2ta02766f>.

[25] X. Chen, G. Wu, J. Chen, X. Chen, Z. Xie, X. Wang, Synthesis of “clean” and well-dispersive Pd nanoparticles with excellent electrocatalytic property on graphene oxide, *J. Am. Chem. Soc.* 133 (2011) 3693–3695, <https://doi.org/10.1021/ja110313d>.

[26] W. Si, Z. Yang, X. Hu, Q. Lv, X. Li, F. Zhao, J. He, C. Huang, Preparation of zero valence Pd nanoparticles with ultra-efficient electrocatalytic activity for ORR, *J. Mater. Chem. A* 9 (2021) 14507–14514, <https://doi.org/10.1039/D1TA00788B>.

[27] W. Jiao, C. Chen, W. You, X. Zhao, J. Zhang, Y. Feng, P. Wang, R. Che, Hollow palladium–gold nanochains with periodic concave structures as superior ORR electrocatalysts and highly efficient SERS substrates, *Adv. Energy Mater.* 10 (2020) 1904072, <https://doi.org/10.1002/aenm.201904072>.

[28] L. Sahoo, R. Garg, K. Kaur, C.P. Vinod, U.K. Gautam, Ultrathin twisty PdNi alloy nanowires as highly active ORR electrocatalysts exhibiting morphology-induced durability over 200 K cycles, *Nano Lett.* 22 (2022) 246–254, <https://doi.org/10.1021/acs.nanolett.1c03704>.

[29] S. John St., R.W. Atkinson, O. Dyck, C.-J. Sun, T.A. Zawodzinski, A.B. Papandrew, Segregated Pt on Pd nanotubes for enhanced oxygen reduction activity in alkaline electrolyte, *Chem. Commun.* 51 (2015) 16633–16636, <https://doi.org/10.1039/C5CC05706J>.

[30] Z. Li, L. Zhai, Y. Ge, Z. Huang, Z. Shi, J. Liu, W. Zhai, J. Liang, H. Zhang, Wet-chemical synthesis of two-dimensional metal nanomaterials for electrocatalysis, *Natl. Sci. Rev.* 9 (2022) 142, <https://doi.org/10.1093/nsr/nwab142>.

[31] M. Luo, Z. Zhao, Y. Zhang, Y. Sun, Y. Xing, F. Lv, Y. Yang, X. Zhang, S. Hwang, Y. Qin, J.-Y. Ma, F. Lin, D. Su, G. Lu, S. Guo, PdMo bimetallic for oxygen reduction catalysis, *Nature* 574 (2019) 81–85, <https://doi.org/10.1038/s41586-019-1603-7>.

[32] Q. Mao, K. Deng, H. Yu, Y. Xu, Z. Wang, X. Li, L. Wang, H. Wang, In situ reconstruction of partially hydroxylated porous Rh metallene for ethylene glycol-assisted seawater splitting, *Adv. Funct. Mater.* 32 (2022) 2201081, <https://doi.org/10.1002/adfm.202201081>.

[33] H. Yu, T. Zhou, Z. Wang, Y. Xu, X. Li, L. Wang, H. Wang, Defect-rich porous palladium metallene for enhanced alkaline oxygen reduction electrocatalysis, *Angew. Chem. Int. Ed.* 60 (2021) 12027–12031, <https://doi.org/10.1002/anie.202101019>.

[34] Z. Wang, S. Xu, M. Li, K. Deng, H. Yu, Y. Xu, X. Li, H. Wang, L. Wang, Polyethyleneimine-functionalized PdOs bimetallic for enhanced oxygen reduction, *Chem. Commun.* 59 (2023) 4511–4514, <https://doi.org/10.1039/d3cc00221g>.

[35] H. Wang, W. Wang, H. Yu, Q. Mao, Y. Xu, X. Li, Z. Wang, L. Wang, Interface engineering of polyaniline-functionalized porous Pd metallene for alkaline oxygen reduction reaction, *Appl. Catal. B Environ.* 307 (2022), 121172, <https://doi.org/10.1016/j.apcatb.2022.121172>.

[36] D. Yu, Q. Liu, B. Chen, Y. Zhao, P. Jia, K. Sun, F. Gao, Twin PdPtIr porous nanotubes as a dual-functional catalyst for oxygen reduction and evolution reactions, *J. Mater. Chem. A* 10 (2022) 11354–11362, <https://doi.org/10.1039/d2ta00459c>.

[37] G.-R. Xu, C.-C. Han, Y.-Y. Zhu, J.-H. Zeng, J.-X. Jiang, Y. Chen, PdCo alloy nanonetworks–polyallylamine inorganic–organic nanohybrids toward the oxygen reduction reaction, *Adv. Mater. Interfaces* 5 (2018) 1701322, <https://doi.org/10.1002/admi.201701322>.

[38] X.-J. Liu, X. Yin, Y.-D. Sun, F.-J. Yu, X.-W. Gao, L.-J. Fu, Y.-P. Wu, Y.-H. Chen, Interlaced Pd–Ag nanowires rich in grain boundary defects for boosting oxygen reduction electrocatalysis, *Nanoscale* 12 (2020) 5368–5373, <https://doi.org/10.1039/D0NR00046A>.

[39] S. Liu, J. Xiao, X.F. Lu, J. Wang, X. Wang, X.W. Lou, Efficient electrochemical reduction of CO₂ to HCOOH over Sub-2 nm SnO₂ quantum wires with exposed grain boundaries, *Angew. Chem. Int. Ed.* 58 (2019) 8499–8503, <https://doi.org/10.1002/anie.201903613>.

[40] H. Huang, H. Jung, H. Jun, D.Y. Woo, J.W. Han, J. Lee, Design of grain boundary enriched bimetallic borides for enhanced hydrogen evolution reaction, *Chem. Eng. J.* 405 (2021), 126977, <https://doi.org/10.1016/j.cej.2020.126977>.

[41] Z. Cui, X. Bai, Highly active and stable Fe/Co/N co-doped carbon-anchored Pd nanoparticles for oxygen reduction reaction, *ACS Appl. Mater. Interfaces* 14 (2022) 9024–9035, <https://doi.org/10.1021/acsmami.1c22058>.

[42] H. Zhang, S. Liu, Z. Wang, X. Li, K. Deng, H. Yu, X. Wang, Y. Xu, H. Wang, L. Wang, Ni-doped hyperbranched PdCu nanocrystals for efficient electrocatalytic borohydride oxidation, *J. Mater. Chem. A* 10 (2022) 24694–24700, <https://doi.org/10.1039/d2ta07066a>.

[43] F. Liu, X. Wang, X. Chen, X. Song, J. Tian, H. Cui, Porous ZnO ultrathin nanosheets with high specific surface areas and abundant oxygen vacancies for acetylacetone gas sensing, *ACS Appl. Mater. Interfaces* 11 (2019) 24757–24763, <https://doi.org/10.1021/acsmami.9b006701>.

[44] J. Liang, Y. Xia, X. Liu, F. Huang, J. Liu, S. Li, T. Wang, S. Jiao, R. Cao, J. Han, H. L. Wang, Q. Li, Molybdenum-doped ordered Li₀PdZn nanosheets for enhanced oxygen reduction electrocatalysis, *SusMat* 2 (2022) 347–356, <https://doi.org/10.1002/sus2.65>.

[45] V. Stamenkovic, B.S. Mun, K.J.J. Mayrhofer, P.N. Ross, N.M. Markovic, J. Rossmeisl, J. Greeley, J.K. Nørskov, Changing the activity of electrocatalysts for oxygen reduction by tuning the surface electronic structure, *Angew. Chem. Int. Ed.* 45 (2006) 2897–2901, <https://doi.org/10.1002/anie.200504386>.

[46] Y. Wang, A.S. Hall, Pulsed electrodeposition of metastable Pd₃₁Bi₁₂ nanoparticles for oxygen reduction electrocatalysis, *ACS Energy Lett.* 5 (2020) 17–22, <https://doi.org/10.1021/acsenergylett.9b02219>.

[47] Q. Yang, L. Shi, B. Yu, J. Xu, C. Wei, Y. Wang, H. Chen, Facile synthesis of ultrathin Pt–Pd nanosheets for enhanced formic acid oxidation and oxygen reduction reaction, *J. Mater. Chem. A* 7 (2019) 18846–18851, <https://doi.org/10.1039/c9ta03945g>.

[48] B.Y. Xia, H.B. Wu, Y. Yan, X.W. Lou, X. Wang, Ultrathin and ultralong single-crystal platinum nanowire assemblies with highly stable electrocatalytic activity, *J. Am. Chem. Soc.* 135 (2013) 9480–9485, <https://doi.org/10.1021/ja402955t>.

[49] J. Liang, S. Li, Y. Chen, X. Liu, T. Wang, J. Han, S. Jiao, R. Cao, Q. Li, Ultrathin and defect-rich intermetallic Pd₂Sn nanosheets for efficient oxygen reduction electrocatalysis, *J. Mater. Chem. A* 8 (2020) 15665–15669, <https://doi.org/10.1039/d0ta01767a>.